



A reduced order electrochemical and thermal model for a pouch type lithium ion polymer battery with $\text{LiNi}_x\text{Mn}_y\text{Co}_{1-x-y}\text{O}_2/\text{LiFePO}_4$ blended cathode



Xueyan Li^a, Song-Yul Choe^{a,*}, Won Tae Joe^b

^a Mechanical Engineering, 1418 Wiggins Hall, Auburn Univ., AL 36849, USA

^b Battery R&D, LG Chem Research Park, Daejeon 305-738, South Korea

HIGHLIGHTS

- Reduced order model for cells with blended cathode of NMC and LFP.
- Model validation with experimental results of voltage, SOC, and heat generation rate.
- Analysis each active material's contribution to cell performance.

ARTICLE INFO

Article history:

Received 20 February 2015

Received in revised form

13 June 2015

Accepted 15 June 2015

Available online 1 July 2015

Keywords:

Lithium battery

Model

Blended cathode

$\text{LiNi}_x\text{Mn}_y\text{Co}_{1-x-y}\text{O}_2$ (NMC)

LiFePO_4 (LFP)

ABSTRACT

$\text{LiNi}_x\text{Mn}_y\text{Co}_{1-x-y}\text{O}_2$ (NMC) and LiFePO_4 (LFP) as a cathode material have been widely employed for cells designed for high power applications. However, NMC needs further improvements in rate capability and stability that can be accomplished by blending it with LFP. Working mechanism of the blended cells is very complex and hard to understand. In addition, characteristics of the blended cells, particularly the plateau and path dependence of LFP materials, make it extremely difficult to estimate the state of charge and state of health using classical electric equivalent circuit models. Therefore, a reduced order model based on electrochemical and thermal principles is developed with objectives for real time applications and validated against experimental data collected from a large format pouch type of lithium ion polymer battery. The model for LFP is based on a shrinking core model along with moving boundary and then integrated into NMC model. Responses of the model that include SOC estimation and responses of current and voltage are compared with those of experiments at CC/CV charging and CC discharging along with different current rates and temperatures. In addition, the model is used to analyze effects of mass ratios between two materials on terminal voltage and heat generation rate.

© 2015 Elsevier B.V. All rights reserved.

1. Introduction

Conversion efficiency of future power systems used in grids or transportation systems can be substantially improved by storing excess energy and retrieving it that would otherwise be dissipated. Particularly, batteries are preferred as energy storage because of their high efficiency during charging and discharging processes as well as their high power and energy density compared to other alternative storage technologies. Among different battery

technologies, the Lithium ion polymer battery (LiPB) is the most preferred technology simply because of its high power density and the high number of cells that are currently being produced for consumer electronics. The same chemistries for electrodes and minimally modified electrolytes can still be used to design cells for high power applications. However, the packaging can be differently. Depending on the method of packaging, batteries can have a cylindrical, prismatic, or pouch shape. Since the current rates are relative high in the applications, heat generated in the cells becomes high, too, which accelerates side reactions and degradations. As a result, a structural design is required, which includes a relatively high heat transfer capability in addition to massive manufacturability. Therefore, the large format pouch cells are widely used for these high power applications.

* Corresponding author.

E-mail addresses: xz10017@auburn.edu (X. Li), choe@auburn.edu (S.-Y. Choe), wontaejoe@lgchem.com (W.T. Joe).

Anodic materials used for those cells are basically carbon graphite, while different cathode materials are chosen to meet performances of the cells, including a blended chemistry [1]. Several basic cathode materials with extra additives have been made to design either high power or energy cells with safe functionalities and long cycle life considering low manufacturing costs. The major materials with structures are as follows; LiFePO_4 (LFP) with one dimensional olivine structure, LiCO_2 (LCO), $\text{LiNi}_x\text{Mn}_y\text{Co}_{1-x-y}\text{O}_2$ (NMC), and $\text{LiNi}_x\text{Co}_y\text{Al}_{1-x-y}\text{O}_2$ (NCA) with two dimensional layered structure, and LiMn_2O_4 (LMO) with three dimensional spinel structure.

Advantages of the LFP are electrochemical and thermal stability compared to others, the safety can be improved. In addition to a long cycle life, a high rate capability employing nanoparticles can be accomplished. However, the materials show a relatively low capacity (160 Ah/kg) along with a low standard voltage of 3.4 V vs. Li in addition to the voltage plateau caused by two-phase transition during lithiation and delithiation in LFP particles [2].

The other materials, LCO, NMC, and NCA with 2D layered structures have a high capacity and a high standard voltage, but do not show electrochemical and thermal stability in operations. LCO shows the lowest thermal stability, especially when overcharged with a voltage that is larger than 4.2 V. Other components like Al and Mn in NCA and NMC can chemically stabilize the cathode, but cycle life and safety still remain incompletely solved [3,4].

Conversely, LMO with 3D spinel structure is promising with technical advantages of high voltage, high power, good safety, and low cost. However, the manganese can be dissolved in electrolytes, which reduces cycle life and deteriorates safety, and the dissolution is accelerated by elevated temperature. In addition, the capacity and energy density are relatively low and their typical values are about 100–120 Ah/kg and 380 Wh/kg, respectively [1].

Analysis above shows that there is no single chemistry for cathode that provides all of requirements for electric vehicle applications. Blending different chemistries is the potential solution for designers to get around drawbacks and maximize the advantages, as summarized in Fig. 1.

1.1. Review of blended cathode materials

Cathode materials of batteries applied for xEVs should ideally facilitate high capacity, power, energy, rate capability along with good safety, long life at low costs. However none of the single cathode materials can meet all of the requirements above as discussed previously. Blended cathode materials can complement each other and achieve better performance than a single parent cathode material.

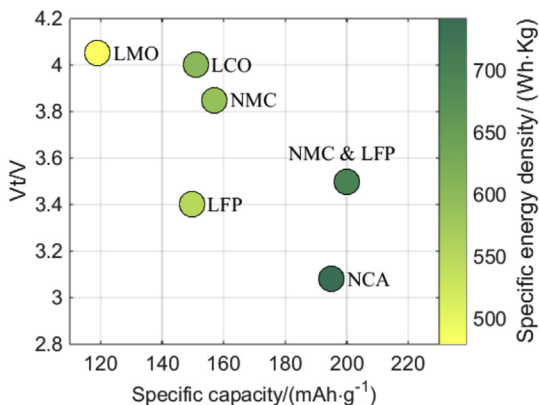


Fig. 1. Performance of cathode materials.

As a matter of fact, LMO is one of favorite cathode materials that can provide high power and rate capability along with increased safety. The demerits of the materials can be improved by blending them with the materials capable of providing high capacity or stabilizing them by preventing from Mn dissolutions. A blended cathode material made of LMO and NCA proposed shows improved performances in increased discharge capacity and reduced heat generation in addition to decreased Mn dissolution. An optimal ratio of NCA for the best performance is 33.3% [5]. In addition, different ratios of LMO and NCA can also achieve improved performances in rate capability, and combined power and energy [6]. Other study shows that blending the LMO with $\text{LiNi}_{0.8}\text{Co}_{0.2}\text{O}_2$ can decrease capacity fade of LMO because of reduced dissolution of Mn into the electrolyte, even at elevated temperatures [7]. The optimal ratio for $\text{LiNi}_{0.8}\text{Co}_{0.2}\text{O}_2$ that completely prevents the dissolution was 15wt%. Structure of cathode materials has been investigated to suppress Mn dissolution and to retain the capacity. The layered oxide cathode such as LCO turned out to be the best performing structure [8]. Contribution of different materials to the cell capacity and structural changes of the mixed LMO and NMC are also investigated using *in situ* X-ray Diffraction (XRD). Based on results for structure changes of each materials during operations, optimal ratio of materials are suggested, which improves the cell capacity [9].

On the other hand, LCO is widely employed as cathode materials for batteries used for portable electronic devices because of high capacity and energy density along with long cycle life. However, poor thermal stability of LCO has raised concerns about safety, especially when being overcharged. This thermal stability can be improved by blending LCO with NMC, whose surfaces are coated with AlF_3 . The modified blended cells show not only improved thermal stability, but also high discharge capacity along with good capacity retention rate [10]. Olivine-structured LFP has been used as an additive for cathode, which also improves the thermal stability of LCO. The LCO/LFP/Al double-layered cathode showed the best tolerance against overcharging and improved safety compared to that of LCO [11].

In addition to the requirements for increased capacity and power density along with high safety, the high rate capability is also an important criteria, which can be achieved using LFP material. LFP as a cathode material has shown a high stability in electrochemical and thermal aspects and a high rate capability, but a low standard potential against Li electrode that is pretty flat around 3.4 V. These drawbacks can be improved by blending it with other materials that have a layered oxide structure.

Two different cathode materials made of LFP/NMC and LFP/LCO are compared each other. The first one has shown superior performance in cycling with high current rates, while the others with layered configuration has shown better in rate capacity because of LCO performance in both good rate capability and high energy density [12]. A different configuration for two materials is proposed, that is made of NMC as the core coated by LFP [13]. The NMC has a high capacity and energy density, but a poor cycle retention at elevated temperature, while LFP has a low energy density but a high thermal stability. The results have shown that the coating using LFP significantly improves cycling performance of NMC at high temperatures without a large initial capacity drop in the first cycle. Furthermore, a blended cathode composed of $x\text{Li}_2\text{MnO}_3 \cdot (1-x)\text{LiNi}_{0.44}\text{Mn}_{0.31}\text{Co}_{0.25}\text{O}_2$ (ANL-NMC, with $x = 0.5$) and LFP is proposed [14], which has increased both energy density and power capability over the entire SOC window because of the low impedance of LFP at low SOC range.

The blended cathodes are a very attractive combination of material that can be used to achieve a better performance than the parent cathode material, with respect to certain operation requirements.

1.2. Review of models for a cell with blended cathode

Since the cathode is made of two different materials, the working mechanism of blended cells is substantially different from that made of a single material, which should be considered in modeling. Generally, behavior of two blended materials is approximated using two different sets of parameters that include particle size, ion diffusivity, conductivity, and equilibrium potential. A model using the two parameter sets has been used to analyze cell performances. Jung [15] studied effects of the different blending ratio between LMO and NMC materials for optimization of cell design. Dai [16] studied effect of blend ratio between LMO and NCA materials on stress generation during cell operation. In addition, interactions between particles that have different radii are modeled using contact resistances present between particles [17]. Similarly, cathode made of NCA and LMO is modeled considering contact resistances between various particles and conductive matrix, which shows improved prediction of terminal responses, particularly at high current rates. The model is used to analyze effects of molar fraction of LMO on energy and power [6].

The active materials used for their modeling efforts have the same intercalation mechanisms. However, the blended cathode with NMC and LFP is difficult to model because of the two-phase transition taking place in LFP particles and has not been modeled yet. In this paper we propose a reduced order electrochemical and thermal model to simulate the performance of cells with graphite anode and NMC/LFP blended cathode. Firstly the modeling principles for two cathode materials are introduced. Secondly the equilibrium potential of the blended cathode regarding to blending

ratio is analyzed. Finally we validate the ROM and analyze the effects of blending ratio on cell performance.

2. Reduced order model (ROM) for cells with blended cathode

Mathematical models for NMC cells and LFP cells were developed separately in previous work [18,19]. The governing equations for the two models are summarized in Table 1, including the mass transport equations in both solid and solution phase, the Ohm's law for both solid and solution phase, the Butler-Volmer equation, the energy equation, and the SOC equation that is derived using ion concentration. The equations for the two models are almost same except the one to calculate ion concentration in solid particles of cathode electrode, because the ion intercalation mechanisms for NMC and LFP particles are different. In addition, two sets of parameters are employed for the two types of cells, including cell geometry, concentration, kinetic, and transport properties.

The model for cells with blended cathode is built based on combination of the two separate models, and modifications are made to treat multiple active cathode materials. For modeling a cell with *n* types of active cathode materials, modifications are made to those equations related to current density, equilibrium potential, and ion concentrations in the solid particles of the cathode electrode.

The total local current flow in the cathode electrode is a sum of the current flow from the two individual active materials, which is calculated using Butler-Volmer equation,

Table 1
Summary of the governing equations for a full order model (FOM) of NMC and LFP cells.

Equation description	Equation for NMC	Equation for LFP
Ion concentration in the solid phase	$\frac{\partial c_s}{\partial t} = \frac{D_s}{r^2} \frac{\partial}{\partial r} \left(r^2 \frac{\partial c_s}{\partial r} \right)$ $\frac{1}{r} \frac{\partial c_s}{\partial r} \Big _{r=0} = 0$ $D_s \frac{\partial c_s}{\partial r} \Big _{r=R_s} = \frac{-j^{Li}}{a_s F}$	$\frac{\partial c_s}{\partial t} = \frac{D_{s,\beta}}{r^2} \frac{\partial}{\partial r} \left(r^2 \frac{\partial c_s}{\partial r} \right); D_{s,\beta} \frac{\partial c_s}{\partial r} \Big _{r=r_1} = 0$ $\frac{\partial c_s}{\partial t} = \frac{D_{s,\alpha}}{r^2} \frac{\partial}{\partial r} \left(r^2 \frac{\partial c_s}{\partial r} \right); D_{s,\alpha} \frac{\partial c_s}{\partial r} \Big _{r=R_s} = \frac{-j^{Li}}{a_s F}$ $(c_{s,\alpha\beta} - c_{s,\beta\alpha}) \frac{dr_0}{dt} = D_{s,\beta} \frac{\partial c_{s,\beta}}{\partial r} \Big _{r=r_0} - D_{s,\alpha} \frac{\partial c_{s,\alpha}}{\partial r} \Big _{r=r_0}$
Ion concentration in the solution phase	$\frac{\partial (e_e c_e)}{\partial t} = \frac{\partial}{\partial x} \left(D_e^{eff} \frac{\partial}{\partial x} c_e \right) + \frac{1 - t_+^0}{F} j^{Li}$ $\frac{\partial c_e}{\partial t} \Big _{x=0} = \frac{\partial c_e}{\partial t} \Big _{x=L} = 0$	
Ohm's law in the solid phase	$\frac{\partial}{\partial x} \left(\sigma^{eff} \frac{\partial}{\partial x} \phi_s \right) - j^{Li} = 0$ $-\sigma^{eff} \frac{\partial \phi_s}{\partial x} \Big _{x=0} = -\sigma^{eff} \frac{\partial \phi_s}{\partial x} \Big _{x=L} = \frac{I}{A} \frac{\partial \phi_s}{\partial x} \Big _{x=L} = \frac{\partial \phi_s}{\partial x} \Big _{x=L+L_{sep}} = 0$	
Ohm's law in the solution phase	$\frac{\partial}{\partial x} \left(\kappa^{eff} \frac{\partial \phi_e}{\partial x} \right) + \frac{\partial}{\partial x} \left(\kappa_D^{eff} \frac{\partial}{\partial x} \ln c_e \right) + j^{Li} = 0$ $\frac{\partial \phi_e}{\partial x} \Big _{x=0} = \frac{\partial \phi_e}{\partial x} \Big _{x=L} = 0$	
Butler-Volmer equation	$j^{Li} = a_s i_0 \left\{ \exp \left[\frac{\alpha_a F}{RT} (\eta - \eta_{SEI}) \right] - \exp \left[-\frac{\alpha_c F}{RT} (\eta - \eta_{SEI}) \right] \right\}$ $\eta = \phi_s - \phi_e - U$	
Energy equation	$\rho C_p \frac{\partial T}{\partial t} = Q_{gen} - q$ $Q_{gen} = \frac{I}{V} \left(U_{OCV} - V_T - T \cdot \frac{\partial U_{OCV}}{\partial T} \right)$ $q = \frac{h}{d} (T - T_{amb})$	
SOC definition	$SOC = \left[\frac{1}{L} \int_0^L \frac{(c_{s,ave} - c_{s,max} \cdot Stoi0)}{c_{s,max} \cdot (Stoi100 - Stoi0)} dx \right] \cdot 100\%$	

$$j_i^{Li} = \sum_{i=1}^n j_i^{Li}$$

$$j_i^{Li} = a_{s,i} i_{0,i} \left\{ \exp \left[\frac{\alpha_a F}{RT} \eta_i \right] - \exp \left[-\frac{\alpha_c F}{RT} \eta_i \right] \right\} \quad (1)$$

$$i_{0,i} = k \cdot (c_e)^{\alpha_a} \cdot (c_{s,max,i} - c_{s,surf,i})^{\alpha_a} \cdot (c_{s,surf,i})^{\alpha_c}$$

$$\eta_i = \phi_s - \phi_e - U_i - R_{contact,i} j_i^{Li}$$

where i represents active material, j_i^{Li} is the current density, a_s is the interfacial surface area, i_0 is the exchange current density, which is a function of ion concentration in electrolyte c_e and solid particles c_s , α_a and α_c are the anodic and cathodic charge transfer coefficient, R is the universal gas constant, T is the temperature, and η is the overpotential defined as the potential difference between the solid ϕ_s , electrolyte ϕ_e and the equilibrium U , and $R_{contact,i}$ is the contact resistance between the solid particle and the conductive matrix.

Due to different particle size, the interfacial surface area of the two materials, a_s , are different, which can be calculated from $3 \varepsilon_s / R_s$. Likewise, the surface overpotentials of the two types of particles are also different because of their different equilibrium potentials determined by the surface ion concentration. As a result, the current density used for all the basic equations in Table 1 should be replaced by the equation derived for the blended cathode.

In addition, the effective conductivity of the blended cathode is a sum of individual conductivity reflecting the volume fraction of the material,

$$\sigma^{eff} = \sum_{i=1}^n \sigma_i \cdot \varepsilon_{s,i} \quad (2)$$

Similar to the SOC definition for cells with a single cathode material mentioned in Table 1, a new equation for SOC is derived based on the principle of charge conservation considering difference in volume fraction, stoichiometry number, and maximum ion concentration of each active material,

$$SOC = 100\% \frac{1}{L_+} \int_0^{L_+} \frac{\sum_{i=1}^n \varepsilon_{s,i} \cdot (c_{s,ave,i} - c_{s,max,i} \cdot Stio_{0,i})}{\sum_{i=1}^n \varepsilon_{s,i} \cdot c_{s,max,i} \cdot (Stio_{100,i} - Stio_{0,i})} dx \quad (3)$$

The energy equation in Table 1 is also updated to calculate heat generation rate in blended cathode, which considers current and overpotential of each active material,

$$Q_{gen.} = \sum_{i=1}^n \frac{I_i}{V} \left(U_{OCV,i} - V_T - T \cdot \frac{\partial U_{OCV,i}}{\partial T} \right) \quad (4)$$

The governing equations above include partial differential equations (PDE) that can be discretized and solved numerically. However, the computational time of the full order model based on the PDEs increases exponentially with increased number of equations. By contrast, the hardware currently being used for battery management systems has a limited performance, so the full order model cannot be implemented. Thus, the model order is further reduced, which includes ion concentrations in both the electrode and the electrolyte, potentials, and kinetics. The reduction of the ion concentration in the electrode and electrolyte is accomplished using the polynomial approach and the state space method, while potentials and electrochemical kinetics are reduced by linearization. In addition, the energy equation is used to calculate the heat generation during cell operation, on which the diffusion coefficients are dependent. Details can be found in the previous paper. The results show that the calculation time of the ROM is

approximately one fifteenth of that of the full order model, while the accuracy can be maintained.

3. Equilibrium potential

The equilibrium potential is dependent upon lithium ion concentration in solid particles and expressed as a function of stoichiometric number. Below are the equilibrium potentials for anode and cathode materials that includes graphite, NMC and LFP, as shown in (5) and plotted in Fig. 2.

$$U_{equ,i} = f_i(x_i), \text{ where } i = \text{Li}_x\text{C, NMC and LFP}$$

$$x_i = \frac{c_{s,i}}{c_{s,max,i}} \quad (5)$$

SOC of each material as well as its capacity can be expressed as a function of stoichiometric number, as shown in (6),

$$SOC_i = \frac{x_i - Stio_{0,i}}{Stio_{100,i} - Stio_{0,i}} \quad (6)$$

$$Capacity_i = (1 - SOC_i) \cdot Capacity_{max,i},$$

where the maximum capacity of NMC and LFP is 157 and 149.6 mAh/g, respectively.

Based on the two equations above, the relationship between capacity and equilibrium potential for a single active material is derived, as the red and purple curves showing in Fig. 3. Using NMC allows for a high operating voltage, but a rapid voltage drop occurs at 3.6 V during discharging. Conversely, the equilibrium potential of LFP is around 3.425 V that is relatively low and constant for most of operating ranges. However, the outputting power is still high even at the end of discharge.

For a cathode made of n types of materials, its resulting equilibrium potential is obtained from the equations above using characteristics and the blending ratio of each material. Under the assumption that the n types of electrode particles are evenly mixed and in contact to each other, the equilibrium potential of all the particles should be the same at any given steady states. As a result, the stoichiometry of each material can be calculated by the inverse function of (5), $x_i = f_i^{-1}(U_{equ,i})$ at any given U_{equ} and then the SOC and capacity of each material can be obtained using equation (6). In addition, the capacity of the blended cathode as well as SOC at a given blending ratio can be calculated as following,

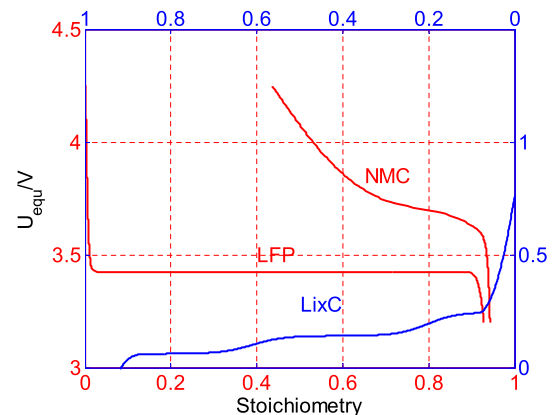


Fig. 2. Equilibrium potential of pure active materials including NMC, LFP, and Li_xC .

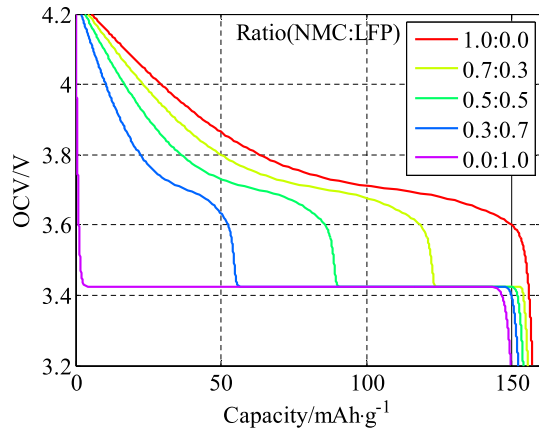


Fig. 3. Equilibrium potential of NMC/LFP blended cathode with different mass ratios of 1:0, 7:3, 5:5, 3:7, and 0:1.

$$Capacity_{cell} = \sum_{i=1}^n Capacity_i \cdot Ratio_i \quad (7)$$

$$SOC_{cell} = 1 - \frac{Capacity_{cell}}{Capacity_{cell,max}}$$

Based on the relationship above, OCV and capacity of a cathode composed of NMC and LFP as a function of its blending ratio are plotted in Fig. 3. Different colors represent different mass ratio between NMC and LFP. Likewise, an equilibrium potential of an anode made of multiple active materials can be calculated.

Once the equilibrium potentials of both cathode and anode are known, the Open Circuit Voltage (OCV) of a cell is given by the difference between the potential of cathode and anode and can also be measured experimentally. The cells used for this study have a graphite anode and a cathode composed of 70% NMC and 30% LFP. On one hand, measurement of the OCV of the cells is carried out using voltage relaxation method. The method starts with an initial state where the battery is fully charged and correspondingly SOC is 100%. Then, the battery is discharged at a 0.1C rate for 1 min and then keep open circuit for 15 min for the cell to be sufficiently relaxed. After the relaxation, the measured terminal voltage is considered to be the OCV at that state. At the same time, SOC is estimated by the Coulomb counting method. This process is repeated until the terminal voltage reaches the cutoff voltage. The measured data of the OCV are plotted with cyan stars in Fig. 4. On the other hand, based on the calculation method above, a predicted OCV from the potential of cathode (yellow solid line) and anode (blue solid line) is plotted and compared with that measured experimentally. The comparison shows relatively good match, so the same method can be also used to calculate the equilibrium potential of a cathode or anode composed of multiple active materials with different blending ratio.

4. Results and analysis

The ROM developed is validated experimentally and ion concentrations in each active material are analyzed. Key specifications of the cell used for the experiments are as follows;

- Materials: Cathode; NMC and LFP, Anode; Carbon,; Electrolyte; organic material, and separator; PE/PP/PE
- The nominal capacity: 41 Ah
- Operation range of the terminal voltage: 2.5 V–4.2 V. 0% SOC to 100% SOC correspond to 2.5 V and 4.2 V at a cutoff current of 2.05 A, respectively.

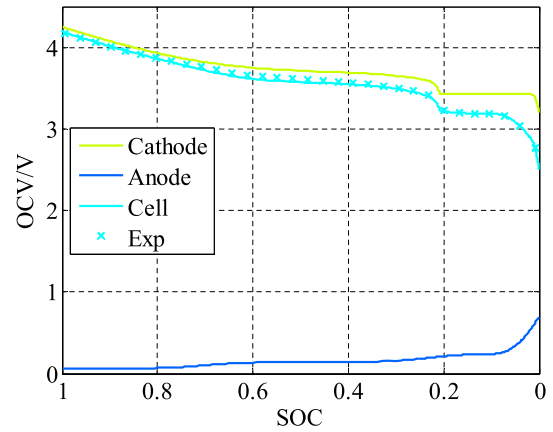


Fig. 4. Calculated and measured equilibrium potential of NMC/LFP blended cathode with mass ratio of 7:3.

A test station is constructed to cycle cells and measure terminal voltage, current and temperature. The cell is placed in a calorimeter in order to keep the cell temperature constant, at the same time, heat generation rate can be measured. The temperature of the cell is the average measurements of three thermal couples placed on the surface of the cell.

Validation of the ROM is performed under following operation conditions, where cells are charged at various current rates of CC/CV mode and discharged at various current rates of CC mode. The ambient temperature ranges is from 10 to 60 °C. The responses of the ROM are compared with the experimental data collected with the test station, which includes terminal voltage, SOC, and temperature. The values of the parameters of the model are listed in Table 2.

4.1. Response of the ROM at different discharging current and a constant room temperature of 25 °C

Three constant discharging current rates of 1C, 2C, and 2.5C are applied to validate the ROM, where an initial SOC is needed as an input parameter. Output variables of the ROM includes the terminal voltage, SOC, current density, heat generation rate and ion concentration. The initial SOC value for the cell is set to be 100%.

The terminal voltage and SOC during discharging as a function of time are plotted in Fig. 5 and Fig. 6, where solid lines and stars represent experimental data and simulation results, respectively. The terminal voltage suddenly drops at the beginning when a step discharging current is applied and then decreases according to a characteristic that follows the characteristic of NMC and finally LFP cells. As expected, the SOC decreases linearly, which can be excellently predicted by the ROM. Analysis of discharging processes in the two different chemistries using the ROM at 1C rate reveals that discharging process takes place in the NMC dominantly until a certain SOC is reached and then in LFP, as shown in Fig. 6, where the blue stars dashed line and dash dot represent the SOC of the cathode, NMC, and LFP, respectively. More details of the contribution of NMC and LFP are show in Fig. 7. Once discharge current is applied, NMC becomes the major contributor for change of the SOC, while LFP remains almost the same as its initial value, when SOC has not reached 30%. When SOC reaches a value around 30%, charges inserted into LFP particles begin to increase and the SOC of LFP drops dramatically until the end of discharge, while the SOC change of NMC becomes much slower. This different discharging behavior of the two materials is caused by the nonlinear dependency of the equilibrium potentials upon stoichiometry

Table 2
List of model parameters (a: Manufacture; b: Validation; c: Estimated.).

Parameter	Negative electrode	Separator	Positive electrode		Unit	
			NMC	LFP		
Electrode plate area, A	23,675		22,290		cm^2	a
Thickness, δ	$100 \cdot 10^{-4}$	$25 \cdot 10^{-4}$	$135 \cdot 10^{-4}$		cm	a
Particle radius, R_s	$8.5 \cdot 10^{-4}$		$3.45 \cdot 10^{-4}$	$5.5 \cdot 10^{-4}$	cm	a
Active material volume fraction, ϵ_s	0.655		0.432	0.258		a
Porosity, ϵ_e	0.32	0.5	0.28			a
Average electrolyte concentration, c_e	0.0123	0.0123	0.0123		mol cm^{-3}	a
Maximum solid phase concentration, $c_{s,\text{max}}$	0.012		0.015	0.007	mol cm^{-3}	c
Diffusion coefficient in solid, D_s	$3.2 \cdot 10^{-10}$		$2.22 \cdot 10^{-9}$	$1.3 \cdot 10^{-9}$	$\text{cm}^2 \text{ s}^{-1}$	b
Diffusion coefficient in electrolyte, D_e	$2.60 \cdot 10^{-6}$	$2.60 \cdot 10^{-6}$	$2.60 \cdot 10^{-6}$			b
Limitation concentration ($c_{s,\alpha\beta}/c_{s,\text{max}}$)			0.02	0.85		b
Stoichiometry at 0% SOC, Stoi_0	0.01		0.9427	0.9284		b
Stoichiometry at 100% SOC, Stoi_{100}	0.87		0.4358	0.0012		b
Contact resistance, R_{contact}	30		400	300	$\Omega \text{ cm}^2$	b
Equilibrium potential of NMC	$3.4245 + 0.85 \cdot \exp(-400 \cdot y^{1.3}) - 17 \cdot \exp(-0.98 \cdot y^{-14})$; $y = c_{s,\text{surf}}/c_{s,\text{max}}$					a,b
Equilibrium potential of LFP	$91.05 \cdot y^6 - 361.4 \cdot y^5 + 561.9 \cdot y^4 - 438.3 \cdot y^3 + 181.4 \cdot y^2 - 43.02 \cdot y + 5872 - 5863 \cdot \exp(5.601 \cdot y^{193.3}) + 0.1$; $y = c_{s,\text{surf}}/c_{s,\text{max}}$					a,b
Equilibrium potential of Li_xC	$(0.1011 - 0.04 \cdot \tanh(13.76 \cdot x - 8.4)) \cdot (x \leq 1) - 252.707 \cdot (x - 0.854)^3 \cdot (x > 0.854 \ \& \ x \leq 1)$; $+ (0.0523 - 0.05275 \cdot \tanh(14.05 \cdot x - 0.856)) \cdot (x \leq 0.4) + (71.43 \cdot (x - 0.085)^2) \cdot (x \leq 0.085)$; $x = c_{s,\text{surf}}/c_{s,\text{max}}$					a,b

number. In fact, the ratio of SOC changing rates of two materials is reversely proportional to that of their equilibrium potentials changing rates. As shown in Fig. 2, for the range of high SOC (low stoichiometry), the equilibrium potential slope of LFP is much higher than that of NMC. As a result the change of SOC in NMC is faster than that in LFP. Likewise, the change of SOC in NMC is slower than that in LFP for a low range of SOC. In addition, different reaction rates of the two materials are another factor that affects not

only SOC of the two materials, but also the terminal voltage during discharging process.

When the cell is discharged with a constant current of 1C rate, there is only α phase inside of LFP particles, and the terminal voltage continuously drops until around 3.2 V, where the plateau

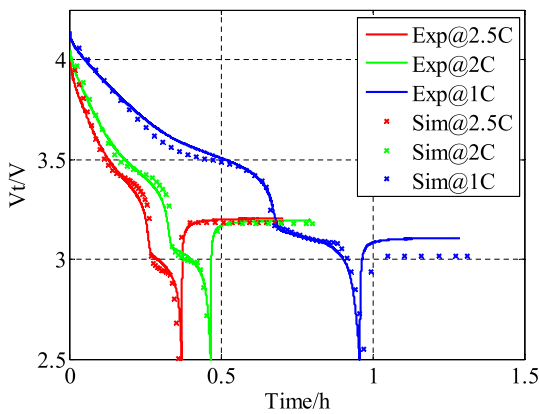


Fig. 5. Comparison of terminal voltage at 1C, 2C, and 2.5C during discharging at 25 °C.

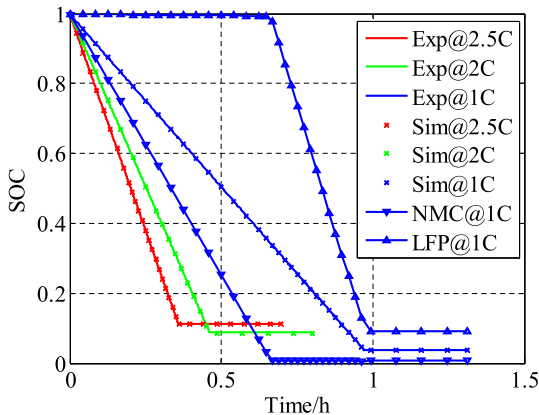


Fig. 6. Comparison of SOC at 1C, 2C, and 2.5C during discharging at 25 °C.

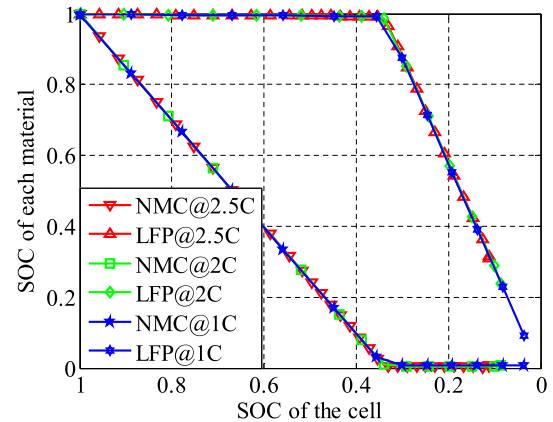


Fig. 7. SOC of each active material in cathode at 1C, 2C, and 2.5C during discharging at 25 °C.

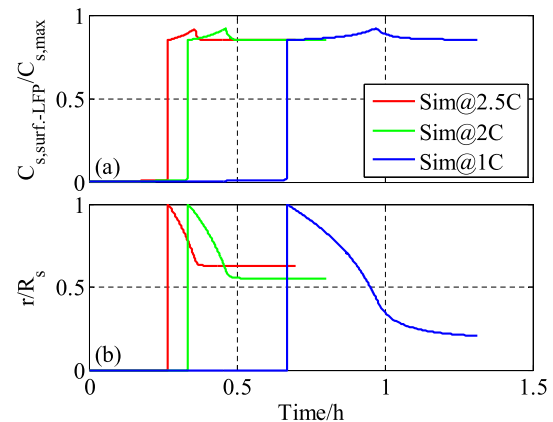


Fig. 8. Ion concentration on the surface of LFP particles and the location of the interface between α and β phase inside of LFP particles at 1C, 2C, and 2.5C during discharging at 25 °C.

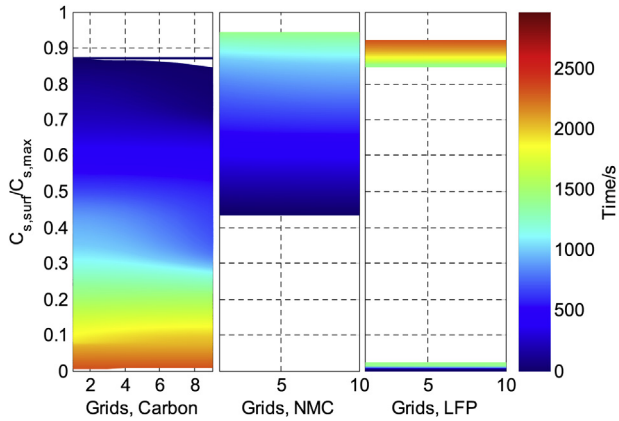


Fig. 9. Simulation results of ion concentration on the surface particles of both the anode and cathode at 2C during discharging at 25 °C.

begins. LFP particles find themselves in the two-phase region. The starting time of the plateau found in Fig. 5 is around 0.7 h, which matches well with the simulation results of ion concentration on the surface of the LFP particles, as shown in (a) of Fig. 8. At around 0.7 h, β phase starts to form on the surface of the LFP particles, and then the interface between the two phases is moving toward the center of particles with discharge going on, until the terminal voltage reaches 2.5 V. The generation and the movement of the interface in LFP particles are shown in (b) of Fig. 8. Before 0.7 h, there is only α phase inside of the particle, so the location of the interface r/R_s is 0. Once β phase starts to be generated, the value of r/R_s becomes 1 and then continues to decrease until the discharging process stops.

More details of the ion concentration in the particles of both negative and positive composite electrodes during 2C discharging are plotted in Fig. 9. The ion concentration on the surface of Li_xC , NMC, and LFP particles are shown from left to right. During discharging process, ion concentration decreases in negative electrode and at the same time increases in positive electrode. Note that there are two regions in the plot of LFP, the lower concentration implies there is only single α phase inside of LFP particles, and the high concentration range implies the generation and growth of β phase in the LFP particles.

Contribution of two active materials in the cathode electrode to the total current is analyzed with 1C rate during discharge. The current density produced from NMC and LFP particles during discharging are plotted in stars and circles in Fig. 10. Similar to the

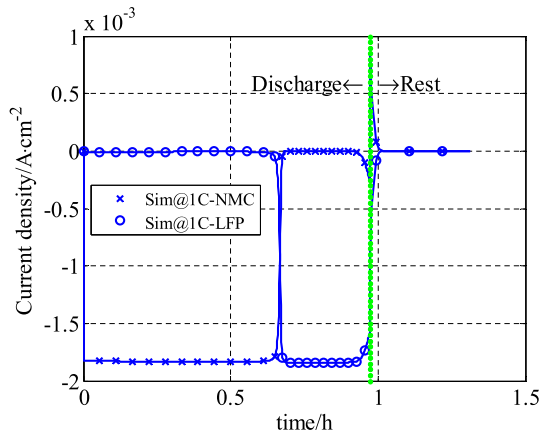


Fig. 10. Current density from NMC and LFP particles at 1C during discharging at 25 °C.

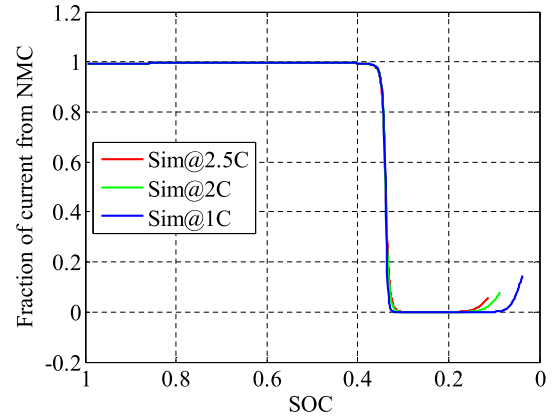


Fig. 11. Current fraction of current from NMC particles at 1C, 2C, and 2.5C rate during discharging at 25 °C.

analysis of SOC, NMC produces high current, while LFP does low current when discharging process starts. When the voltage drops below 3.2 V, LFP actively produces high current while the current from NMC suddenly drops to a very small value near 0 until the end of discharge process.

The current fraction from NMC at different current rates are plotted in Fig. 11. A sudden drop of the current from NMC was observed for all cases, which is directly related to the sudden drop of the terminal voltage, as shown in Fig. 5. In fact, active participation of the two different materials on cathode in intercalation or deintercalation processes depends upon the equilibrium potential of two materials.

If the potentials at a given SOC on the surface of both particles are greater than around 3.425 V given by LFP potential, then NMC is actively participating in intercalation process. Otherwise, LFP is actively participating in the process. Consequently, the current fraction from LFP is small and almost zero at high SOC range, while the current fraction from NMC is small, but larger than zero at low SOC. Particularly, the current fraction from NMC tends to increase at high current rates, when the terminal voltage is approaching to 2.5 V. Initial conditions are that SOC is 100% and ions in both NMC and LFP particles are evenly distributed. When a discharging current is applied, ion concentration gradient within NMC particles is formed in radial and through-the-plane direction. The gradients of ion concentration in NMC particles continuously grow until LFP particles dominantly become in charge of main reaction for intercalation. Then, the gradients become small and as a result the overpotential decreases because of diffusion, which results in more ions accepted by NMC particles. The larger the current is applied, the larger becomes the concentration overpotential, which leads to a high ion acceptance by NMC particles at low SOC range.

Capacity of each material as a function of c rates is calculated with the ROM based on integration of currents and plotted in Fig. 12, where green and cyan bar represent the capacity of NMC and LFP, respectively. Generally the capacity of the active material decreases when current increases, because a high current induces high ohmic and concentration overpotential. However, the plot shows that the capacity of NMC remains almost the same regardless of C rates, while the capacity of LFP depends upon C rates, which implies NMC can be better utilized when blending with LFP. Therefore, the rate capability of blended cells can be improved compared to that of cells with a single cathode material.

Discharging process stops for all three cases when the terminal voltage reaches 2.5 V and then cells are rested for 1200s long. When the discharging current is interrupted, no current flows from anode

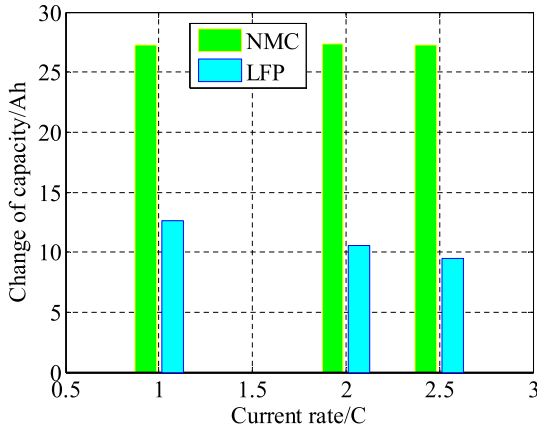


Fig. 12. Capacity change of NMC and LFP particles at 1C, 2C, and 2.5C rate during discharging at 25 °C.

to cathode. However, there are ionic currents flowing between particles until an equilibrium state is reached. As shown in the right part of Fig. 10, current of NMC is positive, while that of LFP is negative, which implies a current flow from LFP particles to NMC particles. During the relaxation, the potentials on the surfaces of all particles in anode or cathode become equivalent levels and subsequently the terminal voltage reach a steady state as shown in Fig. 4. Hence, the ions are evenly distributed in carbon and NMC particles, the interface inside of LFP particles stops moving as shown in Fig. 8.

The simulation results of terminal voltage during relaxation matches well with experimental data after 2.5C and 2C discharging, while a slight discrepancy after 1C discharging is observed. The total discharging time of simulation is longer than that of experiment, which leads to lower SOC and lower OCV of the simulation result.

4.2. Response of the ROM at different charging currents and a constant room temperature of 25 °C

Likewise, the charging behavior of the blended cell is analyzed using the ROM under different CC and CV charging conditions. Simulated terminal voltage are compared with experimental data, as shown in Fig. 13 and Fig. 14. In contrast to discharge, when a charging process starts, LFP particles release charges at the first, while NMC particles do not participate at the first moment, which are more obvious in analysis of SOC of the two particles as shown in

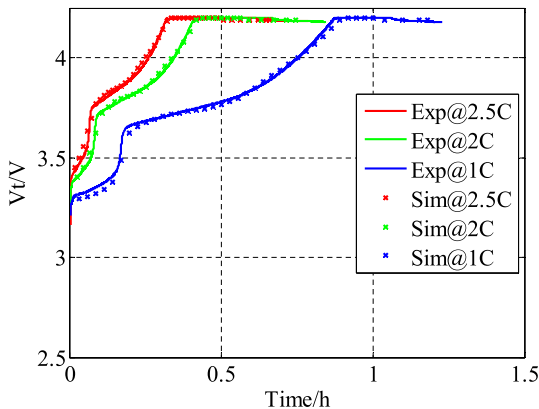


Fig. 13. Comparison of terminal voltage at 1C, 2C, and 2.5C during charging at 25 °C.

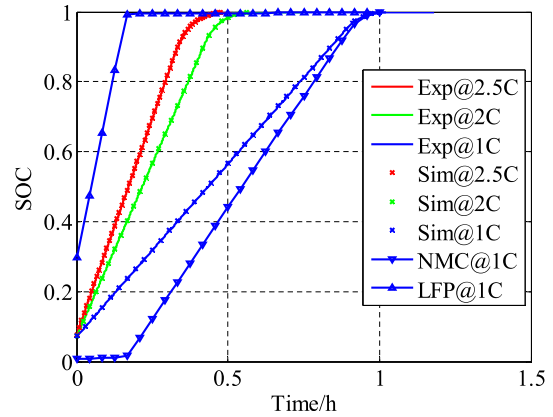


Fig. 14. Comparison of SOC at 1C, 2C, and 2.5C during charging at 25 °C.

Fig. 14.

In addition, ion concentration on the surface of LFP particles and the location of the moving interface between the two-phase in the LFP particles are plotted in (a) and (b) in Fig. 15. The initial SOC of the cell before charging is set to be 10%. Ions in the particles are evenly distributed within the two-phase region, where β and α phase are in the shell and core. The initial interface is located at 0.62 of the particle's radius. When the charging current is applied, α phase is generated on the surface of the particles, which results in a generation of the second interface. As a result, three layers inside of the particle are formed and two interfaces coexist, which is $\alpha/\beta/\alpha$ from the shell to the core. Since there is no ion concentration gradient around the first interface, it stays as before; but the second interface is in motion because of decreasing amount of ions in the outer layer. As ion concentration in α phase decreases, the layer of α phase is getting thicker and the second interface moves toward the first interface. As a result, r/R_s decreases to less than 1. When the second interface meets the first interface, where r/R_s is 0.67, β phase completely disappears and only α phase is left inside of the particle. Then r/R_s drops to 0, and there exists only α phase inside of the LFP particles.

4.3. Response at different ambient temperatures

When cells are charged and discharged, heat is generated and transferred to ambient. Temperatures on the surface of the cells

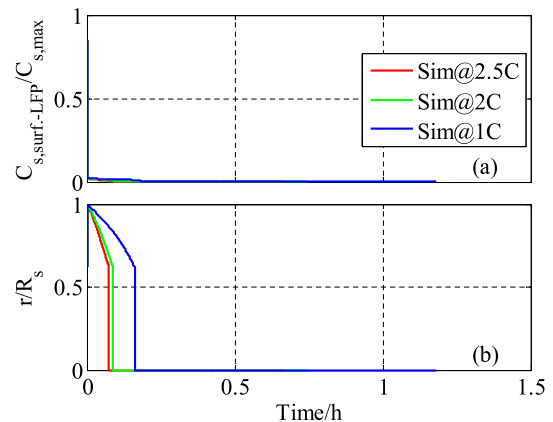


Fig. 15. Ion concentration on the surface of LFP particles and the location of the interface between α and β phase inside of LFP particles at 1C, 2C, and 2.5C during charging at 25 °C.

measured by infrared camera are used to analyze heat generation rates. However, the amount of heat generated is not easy to accurately measure. Therefore, a calorimeter is designed using two thermal-electric-modules, which facilitates dynamic measurements of heat generated during discharging and charging processes. The heat generated in a cell is described based on the energy equation of (4) that does not take heat of mixing [20] into account. Comparison between simulations (solid lines) and experiments (dotted lines) are plotted in Fig. 16 and Fig. 17. During discharging, the ROM can predict the measured heat generation, except the discrepancy at the end of discharging caused by mismatch of terminal voltage as shown in Fig. 5. Even for the period of relaxation, heat is continuously generated because of ionic currents flowing within and among particles. Since ROM does not consider gradient of ion concentrations within particles, heat generation after a current interruption becomes immediately zero [20]. During charging process, a discrepancy between the simulations and experiments is observed at the beginning of charging, which is caused by the increased overpotential of LFP during charging.

Heat generation of the blended cells are strongly affected by characteristic of two active materials. During both discharging and charging, there are two peaks of heat generation rate. The first one is produced when NMC are almost saturated and LFP becomes a dominant part for chemical reactions. The second one is formed at the very end of the discharging process, when LFP are almost saturated and carbons are almost depleted. Accordingly, two peaks of heat generation rate are experimentally and theoretically

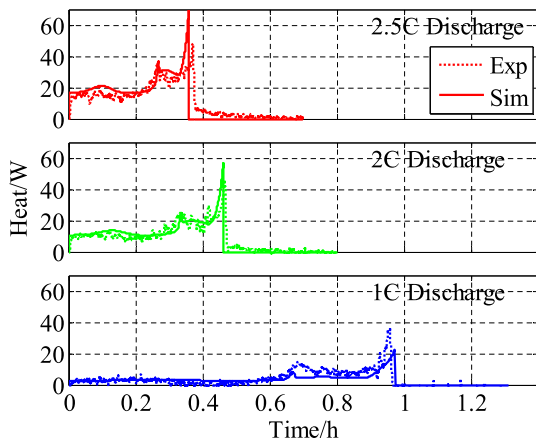


Fig. 16. Heat generation at 1C, 2C, and 2.5C during discharging at 25 °C.

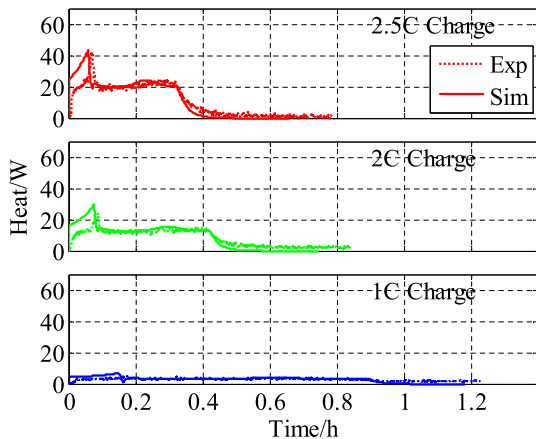


Fig. 17. Heat generation at 1C, 2C, and 2.5C during charging at 25 °C.

observed. The first and the second one are corresponding to instants when ions in NMC and LFP are saturated, respectively, and are determined by the mass ratio of NMC material.

The ROM validated at 25 °C is further developed at different ambient temperatures. Cells are placed in a thermal chamber to keep the ambient temperature constant. At the same time, small current rates are applied to minimize effects of the generating heat on the cell performance during discharging. Comparison between simulated and experimental terminal voltage at different ambient temperatures is plotted in Fig. 18, where the diffusion coefficient of NMC and graphite are fitted to experimental data using exponential functions, as shown in Fig. 19, and incorporated into the ROM aforementioned. Sensitivity analysis of parameters on performance shows no significant dependence of temperature on diffusion coefficient of LFP, which can also be seen from the terminal voltage during 0.1C discharging at different temperatures. As shown in Fig. 20, starting from 100% SOC, the terminal voltage at different ambient temperatures shows a big difference at around 8 h, which corresponds to saturation of NMC, and a small difference at the end of discharging. It also implies the NMC and graphite is more sensitive to temperature than LFP.

4.4. Effects of mass ratio on discharge performance

In section 3, the effect of mass ratio on the equilibrium potential of the blended cathode is analyzed. Likewise, performances of cells

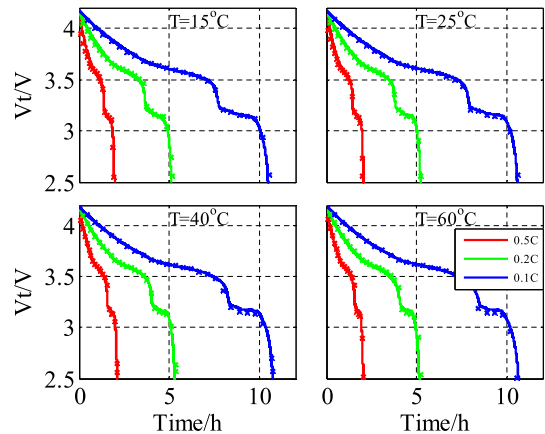


Fig. 18. Experimental (solid line) and simulated terminal voltage (dotted line) during discharging at 0.1C, 0.2C and 0.5C rate and different ambient temperatures of 15, 25, 40, and 60 °C.

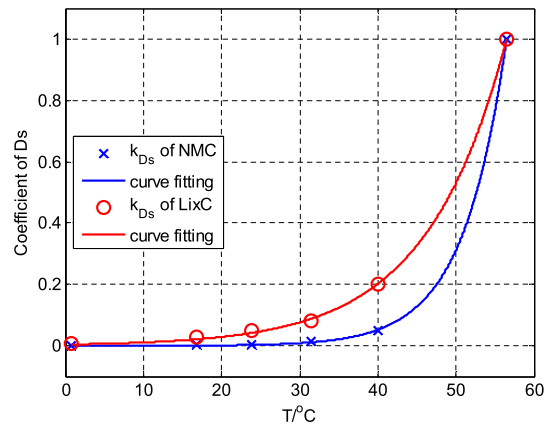


Fig. 19. Diffusion coefficient versus temperature.

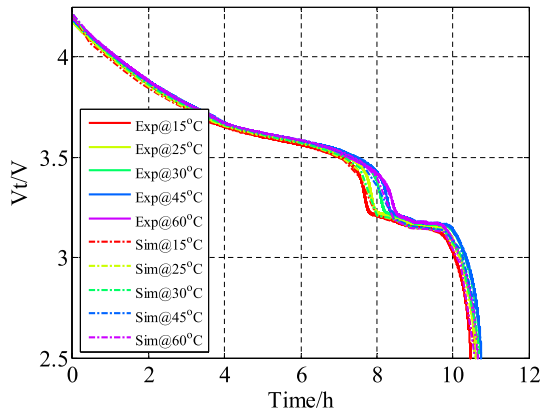


Fig. 20. Experimental (solid line) and simulated terminal voltage (dotted line) during discharging at 0.1C rate and different ambient temperatures of 15, 30, 45, and 60 °C.

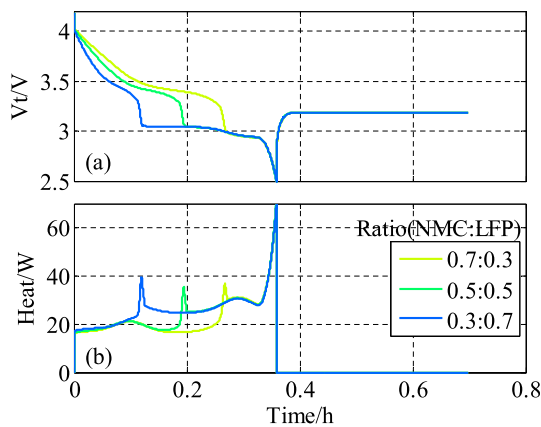


Fig. 21. Comparison of terminal voltage (a) and heat generation rate (b) at 2.5C during discharging at 25 °C with different mass ratio between NMC and LFP.

can be analyzed as a function of the mass ratio of active materials. Effects of the ratio on terminal voltage and heat generation rate is shown in (a) and (b) Fig. 21. The high the ratio of LFP is, the longer becomes the plateau in terminal voltage. At the same time, the magnitude of two peaks of heat generation becomes large and appears early because the saturation of ions in NMC occurs at the first. The blending ratio of multiple active materials is an important factor for design of cells that significantly changes characteristics of cell performances, which can be predicted using the developed ROM.

5. Conclusion

A reduced order electrochemical and thermal model for a high power pouch type cell with blended cathode of NMC and LFP is developed and validated against experimental data. The model is based on two separate sub-models for NMC and LFP cell that have been previously developed. Integration of the two models are successfully conducted considering current distributions, different equilibrium potentials, heat generation rate and blending ratio. The model is capable of predicting static and transient behaviors of the cell during both charging and discharging at various constant current rates and various ambient temperatures, which include terminal voltage and SOC in addition to other internal variables, such as current density, ion concentration in each active material, potentials of both electrode, even generation of new phase and moving of the interface between two phases in LFP material, and

heat generation rate. These variables are essential for optimization of cell design and operation. Here are a summary of major findings.

1. NMC material can be better utilized by blending it with LFP material.
2. The analysis of SOC, ion concentration and current density in each cathode material shows that during both charging and discharging NMC materials play a dominant role in reaction at high SOC range, while LFP is dominant at low SOC range.
3. Mass ratio between NMC and LFP significantly affects terminal voltage and heat generation.

Future work will include development of a model for degradation and its integration into the model and prediction of capacity and power available.

Acknowledgment

This project is funded by LG Chem Ltd. The authors do appreciate the financial support and technical discussions.

Nomenclatures

A	sandwich area of the cell (cm^2)
a_s	specific surface area of electrode (cm^{-1})
c	ion concentration in solid phase (mol L^{-1})
C_p	heat capacity ($\text{J kg}^{-1} \text{K}^{-1}$)
D	diffusion coefficient in electrode ($\text{cm}^2 \text{s}^{-1}$)
d	cell thickness (cm)
E_a	activation energy (kJ mol^{-1})
F	Faraday constant ($96,487 \text{C mol}^{-1}$)
h	convective heat transfer coefficient (W K^{-1})
I	current of the cell (A)
i_0	exchange current density of intercalation (A cm^{-2})
j^{Li}	reaction rate of intercalation (A cm^{-3})
L	thickness of the micro cell (cm)
m	mass of a single cell (kg)
OCV	open circuit voltage (V)
Q	capacity of the cell (An h)
Q_{gen}	heat generation rate (W cm^{-3})
Q_{max}	maximum capacity of the cell (Ah)
q_{ave}	volume-averaged concentration flux (mol cm^{-4})
R	resistance (Ωcm^2) or universal gas constant ($8.3143 \text{J mol}^{-1} \text{K}^{-1}$)
R_s	radius of spherical electrode particle (cm)
r	coordinate along the radius of electrode particle (cm) or location of the interface between α and β phase in LFP particles
SOC	state of charge
T	cell temperature (K)
T_{amb}	ambient temperature (K)
t	time (s)
t^0_+	transference number
U_{equ}	equilibrium potential (V)
V_t	terminal voltage of cell (V)

Greek symbols

α	transfer coefficient of reaction
δ	thickness (mm)
ε	volume fraction
ϕ	electrical potential (V)
η	overpotential (V)
κ	ionic conductivity (S cm^{-1})
λ	eigenvalue
κ_D	concentration driven diffusion conductivity (A cm^{-1})

ρ	density (g cm^{-3})
σ	conductivity (S cm^{-1})

Subscripts

Ave	average
cell	single cell
e	electrolyte phase
max	maximum
n	negative electrode (anode)
p	positive electrode (cathode)
r	radial direction in electrode particle
s	solid phase (active material)
surf	Surface of electrode particle
α	α phase
β	β phase
0%	0% state of charge
100%	100% state of charge
–	negative electrode (anode)
+	positive electrode (cathode)

Superscripts

eff	effective
Li	lithium ion

References

- [1] S.B. Chikkannanavar, D.M. Bernardi, L. Liu, A review of blended cathode materials for use in Li-ion batteries, *J. Power Sources* 248 (2014) 91–100.
- [2] W.-J. Zhang, Structure and performance of LiFePO_4 cathode materials: a review, *J. Power Sources* 196 (2011) 2962–2970.
- [3] N. Yabuuchi, T. Ohzuku, Novel lithium insertion material of $\text{LiCo}_{1/3}\text{Ni}_{1/3}\text{Mn}_{1/3}\text{O}_2$ for advanced lithium-ion batteries, *J. Power Sources* 119 (2003) 171–174.
- [4] A. Hashem, A. Abdel-Ghany, A. Eid, J. Trottier, K. Zaghib, A. Mauger, C. Julien, Study of the surface modification of $\text{LiNi}_{1/3}\text{Co}_{1/3}\text{Mn}_{1/3}\text{O}_2$ cathode material for lithium ion battery, *J. Power Sources* 196 (2011) 8632–8637.
- [5] H.Y. Tran, C. Täubert, M. Fleischhammer, P. Axmann, L. Küppers, M. Wohlfahrt-Mehrens, LiMn_2O_4 Spinel/ $\text{LiNi}_{0.8}\text{Co}_{0.15}\text{Al}_{0.05}\text{O}_2$ blends as cathode materials for lithium-ion batteries, *J. Electrochem. Soc.* 158 (2011) A556–A561.
- [6] P. Albertus, J. Christensen, J. Newman, Experiments on and modeling of positive electrodes with multiple active materials for lithium-ion batteries, *J. Electrochem. Soc.* 156 (2009) A606.
- [7] T. Numata, C. Amemiya, T. Kumeuchi, M. Shirakata, M. Yonezawa, Advantages of blending $\text{LiNi}_{0.8}\text{Co}_{0.2}\text{O}_2$ into $\text{Li}_{1-x}\text{Mn}_{2-x}\text{O}_4$ cathodes, *J. Power Sources* 97–98 (2001) 358–360.
- [8] A. Manthiram, W. Choi, Suppression of Mn dissolution in Spinel cathodes by trapping the protons within layered oxide cathodes, *Electrochem. Solid-State Lett.* 10 (2007) A228.
- [9] K.-W. Nam, W.-S. Yoon, H. Shin, Y.C. Kyung, S. Choi, X.-Q. Yang, In situ X-ray diffraction studies of mixed LiMn_2O_4 - $\text{LiNi}_{1/3}\text{Co}_{1/3}\text{Mn}_{1/3}\text{O}_2$ composite cathode in Li-ion cells during charge-discharge cycling, *J. Power Sources* 192 (2009) 652–659.
- [10] K.S. Lee, S.T. Myung, D.W. Kim, Y.K. Sun, AlF_3 -coated LiCoO_2 and $\text{Li}[\text{Ni}_{1/3}\text{Co}_{1/3}\text{Mn}_{1/3}]\text{O}_2$ blend composite cathode for lithium ion batteries, *J. Power Sources* 196 (2011) 6974–6977.
- [11] N. Imachi, Y. Takano, H. Fujimoto, Y. Kida, S. Fujitani, Layered cathode for improving safety of Li-ion batteries, *J. Electrochem. Soc.* 154 (2007) A412.
- [12] J.F. Whitacre, K. Zaghib, W.C. West, B.V. Ratnakumar, Dual active material composite cathode structures for Li-ion batteries, *J. Power Sources* 177 (2008) 528–536.
- [13] S.-B. Kim, K. Lee, W. Choi, W.-S. Kim, I. Jang, H. Lim, Y. Lee, Preparation and cycle performance at high temperature for $\text{Li}[\text{Ni}_{0.5}\text{Co}_{0.2}\text{Mn}_{0.3}]\text{O}_2$ coated with LiFePO_4 , *J. Solid State Electrochem.* 14 (2010) 919–922.
- [14] K.G. Gallagher, S.H. Kang, S.U. Park, S.Y. Han, $x\text{Li}_2\text{MnO}_3(1-x)\text{LiMO}_2$ blended with LiFePO_4 to achieve high energy density and pulse power capability, *J. Power Sources* 196 (2011) 9702–9707.
- [15] S. Jung, Mathematical model of lithium-ion batteries with blended-electrode system, *J. Power Sources* 264 (2014) 184–194.
- [16] Y. Dai, L. Cai, R.E. White, Simulation and analysis of stress in a Li-ion battery with a blended LiMn_2O_4 and $\text{LiNi}_{0.8}\text{Co}_{0.15}\text{Al}_{0.05}\text{O}_2$ cathode, *J. Power Sources* 247 (2014) 365–376.
- [17] D.E. Stephenson, E.M. Hartman, J.N. Harb, D.R. Wheeler, Modeling of particle-particle interactions in porous cathodes for lithium-ion batteries, *J. Electrochem. Soc.* 154 (2007) A1146–A1155.
- [18] X. Li, M. Xiao, S.-Y. Choe, Reduced order model (ROM) of a pouch type lithium polymer battery based on electrochemical thermal principles for real time applications, *Electrochim. Acta* 97 (2013) 66–78.
- [19] X. Li, M. Xiao, S.-Y. Choe, W.T. Joe, Modeling and analysis of LiFePO_4 /Carbon battery considering two-phase transition during galvanostatic charging/discharging, *Electrochim. Acta* 155 (2014) 447–457.
- [20] M. Xiao, S.-Y. Choe, Theoretical and experimental analysis of heat generations of a pouch type LiMn_2O_4 /carbon high power Li-polymer battery, *J. Power Sources* 241 (2013) 46–55.